Microsc. Microanal. 13, 272–284, 2007
DOI: 10.1017/S1431927607070675

Microscopy AND Microanalysis

Comparison of Compositional and Morphological Atom-Probe Tomography Analyses for a Multicomponent Fe-Cu Steel

R. Prakash Kolli[1,*] and David N. Seidman[1,2]

[1]*Department of Materials Science and Engineering, Northwestern University, Evanston, IL 60208-3108, USA*
[2]*Northwestern University Center for Atom-Probe Tomography (NUCAPT), Northwestern University, Evanston, IL 60208-3108, USA*

Abstract: A multicomponent Fe-Cu based steel is studied using atom-probe tomography. The precipitates are identified using two different methodologies and subsequent morphological and compositional results are compared. The precipitates are first identified using a maximum separation distance algorithm, the envelope method, and then by a concentration threshold method, an isoconcentration surface. We discuss in detail the proper selection of the parameters needed to delineate precipitates utilizing both methods. The results of the two methods exhibit a difference of 44 identified precipitates, which can be attributed to differences in the basis of both methods and the sensitivity of our results to user-prescribed parameters. The morphology of the precipitates, characterized by four different precipitate radii and precipitate size distribution functions (PSDs), are compared and evaluated. A variation of less than ~8% is found between the different radii. Two types of concentration profiles are compared, giving qualitatively similar results. Both profiles show Cu-rich precipitates containing Fe with elevated concentrations of Ni, Al, and Mn near the heterophase interfaces. There are, however, quantitative disagreements due to differences in the basic foundations of the two analysis methods.

Key words: precipitate morphology, concentration profiles, atom-probe tomography, maximum separation distance, envelope method, proxigram, Fu-Cu steel, high-strength low-carbon (HSLC) steel

Introduction

Analysis of atom-probe tomographic (APT) data has historically been time intensive and often involves customized software that provides visual reconstructions, concentrations, morphologies, and positional analyses of internal features, such as clusters or precipitates. Although the desired results are the same, the applied methodologies are often quite different. Commonly used methods to study precipitation in APT data sets include volumetric searches, compositional thresholds, searches for clusters of atoms based on a separation distance(s), and radial distribution functions (RDFs), which each have their own advantages and disadvantages and provide different quantitative results (Hellman et al., 2000, 2002, 2003; Hyde & English, 2000; Miller, 2000*a*; Al-Kassab, 2002; Heinrich et al., 2003; Vaumousse et al., 2003; Miller & Kenik, 2004; Vurpillot et al., 2004; de Geuser et al., 2006; Sudbrack et al., 2006*a*).

The terms cluster and precipitate possess distinct physical meanings within the discipline of physical metallurgy in terms of nucleation, growth, and coarsening models in a multiphase multicomponent system (Christian, 2002). A cluster refers to an agglomeration of atoms forming as a result of random solid-state concentration fluctuations. At a critical dimension, which is a function of the net reversible work to make a nucleus, the cluster becomes stable and it is denoted a nucleus and this is a precipitate. An unstable cluster is denoted an embryo. A nucleus (precipitate) will then undergo growth and coarsening (Ratke & Voorhees, 2002). We also note that in terms of identification of precipitates for atom-probe data, the term cluster also denotes a grouping of atoms that can either be a cluster or a precipitate in terms of nucleation, growth, and coarsening models.

In this investigation two different precipitate identification methodologies, the maximum separation distance envelope method (known as the envelope method) (Hyde, 1993; Miller, 2000*a*, 2000*b*; Miller & Kenik, 2004), and a

Received March 20, 2006; accepted April 20, 2007.
*Corresponding author. E-mail: p-kolli@northwestern.edu

Table 1. Composition of High-Strength Low-Carbon Steel

	Cu	C	Al	Ni	Si	Mn	Nb	P	S
wt%	2.09	0.045	0.68	2.83	0.51	0.50	0.065	0.010	0.003
at.%	1.82	0.209	1.38	2.67	1.00	0.51	0.038	0.018	0.005

concentration threshold method, an isoconcentration surface (Hellman et al., 2000, 2002, 2003), are applied to LEAP tomographic data obtained from a multicomponent high-strength low-carbon (HSLC) Fe-Cu based steel containing chemically complex precipitates (Isheim et al., 2006*a*, 2006*b*). This HSLC Fe-Cu based steel is being developed at Northwestern University for specific use as an explosion-resistant steel for the U.S. Navy (Vaynman et al., 2004*a*, 2004*b*, 2006). The two methodologies are reviewed and the morphologies and compositions of the precipitates isolated by these two techniques are evaluated and compared.

Materials and Methods

Alloy Details

A 45.5-kg (100-lb) heat of an HSLC Fe-Cu based steel was vacuum induction melted and cast at Mittal Steel Research Center, East Chicago, Indiana. The heat was hot-rolled to 12.5 mm (1/2 in.) thick and air-cooled. The bulk composition of this HSLC steel was determined by spectrographic analysis at Mittal Steel Research Center and is given in Table 1. The plates were cut into rods 12.5 mm × 12.5 mm × 250 mm using an abrasive saw and solutionized at 900°C for 40 min and quenched into water at 25°C. The rods were next cut into 12.5 mm × 12.5 mm × 25 mm blocks, which were aged at 500°C for 1 h and then quenched into water at 25°C.

Experimental Details

The blocks were further reduced to 0.3 mm × 12.5 mm × 25 mm coupons, and APT tip blanks ($0.3 \times 0.3 \times 25$ mm^3) were cut from the coupons and electropolished using a two-step procedure (Krakauer et al., 1990; Krakauer & Seidman, 1992). Initial electropolishing was performed with a solution of 10 vol% perchloric acid in acetic acid at 15–10 Vdc at room temperature. This was followed by a manually controlled pulsed final polishing step, using a solution of 2 vol% perchloric acid in butoxyethanol at 8–5 Vdc at room temperature producing a tip with a radius <50 nm. LEAP tomography (Kelly et al., 1996, 2004; Kelly & Larson, 2000) was performed at a specimen temperature of 50 K and at an ultrahigh vacuum gauge pressure of 1.05×10^{-8} Pa (7.88×10^{-11} torr). The pulse rate was 2×10^5 Hz and the pulse-voltage-to-standing-dc-voltage ratio (pulse fraction) was 20%. The data are analyzed using the Imago Visualization and Analysis Software (IVAS). The APT reconstruction is $50 \times 48 \times 24$ nm^3 in volume and contains ca. 1.8 million atoms. The same atomic reconstruction was also imported into the Adam 1.5 program developed at Northwestern University (Hellman et al., 2002) for additional analyses.

Envelope Methodology

The maximum separation distance algorithm (Hyde, 1993) is a methodology for identifying precipitates in an alloy. This algorithm can be used to search for clusters of selected solute atom(s).[1] The basic technique is a recursive search for solute atoms based on the fact that the maximum separation distance, d_{max}, between selected solute atoms is expected to be closer within a precipitate than in the matrix due to a lower concentration in the latter. A second user-defined parameter, the minimum number of solute atoms, N_{min}, defines the cluster of atoms as a precipitate. The specifics of this genre of algorithms have been explained in detail elsewhere (Hyde & English, 2000; Al-Kassab, 2002; Heinrich et al., 2003; Kluthe et al., 2003; Wolde-Giorgis et al., 2003; Miller & Kenik, 2004). The advantages of this method are the ease of automation, the ability to analyze very small precipitates, even ≤1.5 nm radius (Al-Kassab, 2002), and analysis of precipitates independent of their morphology. This method has, however, four major disadvantages: (1) It cannot easily define the precipitate/matrix heterophase interface and may include matrix atoms as part of a precipitate; (2) in cases where the partitioning ratio of solute atoms is close to unity, that is, the solute atoms do not segregate strongly to either the precipitate or matrix, such as occurs in some Ni-Cr-Al alloys (Sudbrack, 2004; Yoon, 2004), the technique would not successfully identify the precipitates; (3) it is sensitive to variations in local detection efficiency; and (4) this method, like others, is sensitive to the parameters chosen by the investigator.

The envelope method (Miller, 2000*a*, 2000*b*; Miller & Kenik, 2004), which is implemented in IVAS by Imago Scientific Instruments, extends the functionality of the maximum separation distance algorithm by defining a third parameter, the grid spacing. The grid spacing permits a three-dimensional grid to be overlaid on the data. Grid cells with solute atoms contained in a precipitate are marked as

[1]Atom-probe tomography detects only ions; however in this article we refer to all detected ions as atoms.

part of the envelope. Unmarked cells within the envelope boundaries are then included, delineating the precipitate. In this manner all elements in the precipitate, whether marked by the maximum separation distance algorithm or not, are included in the precipitate, and analyses of composition and morphology can then be made.

The quantities $d_{\max}$ and $N_{\min}$ are clearly critical for defining properly precipitate morphology and composition (Miller, 2000*b*; Al-Kassab, 2002; Vaumousse et al., 2003; Miller & Kenik, 2004). The values of both parameters can be chosen relative to the solute concentration of the system, the lattice interplanar spacing, the composition of the precipitates, and the efficiency of the multichannel plate detector used in the LEAP tomograph. The quantity $d_{\max}$ must be chosen carefully, as too large a value results in solute atoms from the matrix being incorrectly assigned to a cluster of atoms. The cluster of atoms therefore appears to be larger than its actual size or adjacent clusters may be combined incorrectly into a single larger feature. If too small a value of $d_{\max}$ is chosen, the cluster may be smaller than its true size or even split artificially into multiple smaller clusters. Vaumousse et al. (2003) give a typical range for $d_{\max}$ of 0.4–1.0 nm and Miller (2000*a*) suggests a range of 0.3–0.7 nm. A reasonable value for $d_{\max}$ can be found by plotting the number of clusters of the selected solute atoms, as a function of the distance $d_{\max}$ between solute atoms. A second methodology is to compare the number of clusters in the specimen with that from computer simulations or actual random solid solutions with the same bulk chemical composition as the aged material (Miller, 2000*b*; Miller et al., 2003; Vaumousse et al., 2003). Such simulations, though, are difficult to perform for commercial alloys with many components as opposed to model alloys with two to four components.

The quantity $N_{\min}$ defines the minimum precipitate size and is used to eliminate clusters of atoms that are *not* delineated as precipitates. The value of $N_{\min}$ is dependent on the choice of $d_{\max}$. For example, when $d_{\max}$ is too large, all atoms in the data set would form a single large feature. Vaumousse et al. (2003) offer a typical range of 10–30 atoms for $N_{\min}$. A reasonable value for $N_{\min}$ can be found by plotting the distribution of clusters as a function of the number of solute atoms for a given value of $d_{\max}$. An approach for more complex alloys is to include all atoms found in the clusters defined by $d_{\max}$. One can also compare the number of clusters in the specimen with that from computer simulations or actual random solid solutions with the same bulk chemical composition as the aged material (Miller, 2000*b*; Miller et al., 2003; Vaumousse et al., 2003).

Isoconcentration Surface Methodology

A concentration threshold method, an isoconcentration surface, is implemented in the Adam 1.5 analysis software program (Hellman et al., 2000, 2002, 2003). Rather than using a maximum separation distance to identify the solute atoms anticipated to be found within a precipitate, the precipitates are defined using a concentration threshold, $c^{threshold}$, based upon the fact that the concentration of the solute atoms within a precipitate is greater than in the matrix. This methodology successfully delineates precipitates with almost any compositional variation and morphology, independent of its concavity or convexity. This method also has the advantage of identifying early-stage phase separation or nucleation, with nuclei as small as 0.45 nm being observed (Sudbrack, 2004; Sudbrack et al., 2006*a*, 2006*b*, 2007; Yoon et al., 2007*a*, 2007*b*). The technique has three major disadvantages: (1) the precipitate dimensions and number density are sensitive to the choice of the quantity $c^{threshold}$, (2) the choice of user-defined parameters affects both positional values of the isoconcentration surfaces and statistical error, and (3) possible convolution of small precipitates located close to large precipitates.

To define properly the isoconcentration surfaces, the user must carefully choose the quantity $c^{threshold}$. The selected value must generate morphologically stable results, meaning small changes in the quantity $c^{threshold}$ should not vary significantly the number of precipitates or their dimensions. If too small a value is chosen for $c^{threshold}$, the precipitates may be larger than their true size, and if too great a value is chosen for $c^{threshold}$, the precipitates may be smaller than their true size. The selection of the threshold concentration value is dependent on the system studied and composition of the precipitates.

The isoconcentration surfaces defining each precipitate are generated employing a concentration space. The specifics of a concentration space are explained in detail elsewhere (Hellman et al., 2000, 2002, 2003). To create the concentration space, however, the user must define the three-dimensional grid spacing, the smoothing transfer function, the delocalization distance, and the confidence sigma value. The selection of grid spacing involves a trade-off between positional error and statistical error; too coarse a grid results in positional error at the interface, whereas too fine a grid results in higher statistical error (Hellman et al., 2000). Hellman et al. (2000) suggest using a grid spacing of 1–3 nm. Each atom within the analyzed volume contributes to the concentration at a grid point dependent on the choice of smoothing transfer function and the delocalization distance. A commonly used transfer function is the Gaussian-like spline function, whose details are given elsewhere (Hellman et al., 2003). The selection of a transfer function width must be balanced with the choice of grid spacing. A narrow transfer function will produce poor statistics, whereas a wide transfer function will result in positional error (Hellman et al., 2000). The delocalization distance is chosen to spread the contribution of each atom to adjacent grid points, effectively smoothing the data and improving the statistical error. A typical ratio of 2:1 to 4:1 for delocalization distance to grid spacing is utilized. Lastly, the confidence sigma value is chosen giving isoconcentration

surfaces with a defined statistical uncertainty (Hellman et al., 2003). Once the concentration space is created, the user can select the quantity $c^{threshold}$ generating the isoconcentration surfaces identifying the precipitates.

Morphological Analysis

Volume Equivalent Radius of a Sphere

The volume of a precipitate can be estimated from

$$V_{precipitate} = \frac{N_{atoms}}{\rho\eta}, \tag{1}$$

where N_{atoms} is the number of atoms within the precipitate, ρ is the theoretical atomic density and is equal to 84.3 atoms nm^{-3} for this HSLC Fe-Cu based steel, and η is the estimated detection efficiency of 0.5 of the LEAP tomograph's multichannel plate detector. The volume equivalent radius of a sphere, r_{volume}, is calculated by equating the volume of the precipitate determined from equation (1) to that of a sphere.

Radius of Gyration

The radius of gyration, l_g, is given by

$$l_g = \sqrt{\frac{\sum_{i=1}^{n} m_i r_i^2}{\sum_{i=1}^{n} m_i}}, \tag{2}$$

where n is the number of atoms in the precipitate, m_i is the mass of an individual atom, and r_i is the distance of an individual atom from a precipitate's center of mass (COM). For precipitates consisting predominantly of one species, this can be simplified to

$$l_g = \sqrt{\frac{\sum_{i=1}^{n} (x_i - \bar{x})^2 + (y_i - \bar{y})^2 + (z_i - \bar{z})^2}{n}}, \tag{3}$$

where $\bar{x}$, $\bar{y}$, and $\bar{z}$ define the COM of a precipitate (Miller, 2000*a*; Miller & Kenik, 2004). The quantity l_g represents a physical dimension, but by definition it does *not* represent the actual physical extent of a precipitate. Therefore, the quantity l_g underestimates the dimension of a precipitate. The radius of gyration, though, can be utilized to calculate the radius, r_{sphere}, from

$$r_{sphere} = \sqrt{\frac{5}{3}}\, l_g, \tag{4}$$

which assumes the precipitate is a spherical body.

Guinier Radius

Miller (2000*a*, 2000*b*; Miller & Kenik, 2004) suggests utilizing l_g to find the Guinier radius, r_G, and provides a simple conversion relation, $r_G = \sqrt{5/3}\, l_g$. This equation does *not* represent an accurate physical interpretation of the data. The correct form is

$$r_G = \sqrt{\frac{3}{5}}\, R, \tag{5}$$

where R is the radius of a spherical body (Guinier, 1963; Fultz & Howe, 2002). This simplified expression for r_G is obtained from the Guinier approximation for the scattered X-ray or neutron intensity at very small angles (Guinier, 1963; Fultz & Howe, 2002). This approximation consists of two parts: $I(0)$, which characterizes the total number of scattering objects, and r_G, which describes the distribution of the objects in relation to their COM and radius of gyration. Equation (5) is derived assuming the scattering objects are homogeneous spherical precipitates with a uniform atomic density. The Guinier radius has the same form as the quantity l_g in Newtonian mechanics (Hibbler, 2001), thereby permitting a comparison of small-angle neutron scattering (SANS) data and APT data. By using the quantity r_G to calculate the quantity R in equation (5), SANS data can be compared to the quantity r_{sphere} calculated from the quantity l_g in equation (4) from APT data (Hyde & English, 2000). Although the two have the same form, direct comparison or conversion of the Guinier radius to the radius of gyration is *not* an accurate physical representation of the data, as the former is obtained from a measurement in reciprocal space, whereas the latter is a measurement in direct space. Therefore we do not utilize the Guinier radius when characterizing precipitate morphology from APT data.

Best-Fit Ellipsoid Radius

The best-fit ellipsoid approximation algorithm (Sudbrack, 2004; Karnesky et al., 2007) is implemented in IVAS by Imago Scientific Instruments. The approximation analyzes the identified precipitates by utilizing an eigenvalue decomposition to approximate the morphology of each precipitate with a best-fit ellipsoid. This results in the major, r_{major}, and two minor, $r_{minor\,1}$ and $r_{minor\,2}$, ellipsoid radii for each precipitate. The ellipsoid volume and an effective ellipsoid radius, $r_{ellipsoid}$, based on a sphere of the same total volume as the ellipsoid can be calculated from

$$r_{ellipsoid} = \sqrt[3]{(r_{major})(r_{minor1})(r_{minor2})}. \tag{6}$$

Additionally, the three ellipsoid radii can be used to determine the major/minor_1, major/minor_2, and the minor_1/minor_2 ratios.

Precipitate Size Distribution Functions

The radii of all the precipitates within the analyzed volume are used to generate scaled precipitate size distribution functions (PSDs) (Sudbrack, 2004; Yoon, 2004; Yoon et al., 2007*a*, 2007*b*) giving the distribution of precipitate radii. The distributions are scaled such that the area under a distribution is equal to unity. The scaling bin width is 0.05 $R/\langle R\rangle$ and the error for the reported mean radii is given by the standard error of the mean.

Compositional Analysis

Radial Concentration Profiles

The concentration profile of an individual precipitate is characterized by a radial concentration profile as implemented in IVAS. The profile is delineated from the COM to a distance of 5 nm utilizing a bin width of 0.1 nm. Subsequently, atoms from the first five bins from the COM outward are used to define the core concentrations of the precipitate improving the statistical error, which is determined from counting statistics.[2]

Proximity Histogram Concentration Profiles

The proximity histogram (proxigram for short) algorithm is implemented in the Adam 1.5 analysis software program (Hellman et al., 2000, 2002). The proxigram, which is a weighted superposition of concentration profiles, is created using the isoconcentration surface as a reference surface. The proxigram is generated by binning individual atoms as a function of distance from the isoconcentration surface and normalizing each bin by the total number of atoms within a bin. Therefore, the proxigram is a one-dimensional plot of local concentrations as a function of distance from the reference isoconcentration surface. The convention we use defines positive distances from the heterophase interface to be into the precipitates, whereas negative distances are within the matrix. The core concentrations are derived from the first two data points within the precipitate, meaning the two data points closest to the center of the precipitates, improving the statistical error.

Partitioning Ratios

The partitioning ratios, κ_i, are defined by $\kappa_i = c_i^p/c_i^m$, where c_i^p is the concentration of element i in the precipitate and c_i^m is the concentration of element i in the matrix. The standard error for κ was determined by standard error propagation methods (Meyer, 1975) of the concentration errors. The partitioning ratios are derived following two methodologies. First, the concentrations are determined from elemental and total atom counts determined by the envelope algorithm. Therefore, all atoms within the precipitates and the matrix, including those at the heterophase interface, are utilized. In the second methodology, the precipitate and matrix concentrations are derived from the precipitate core concentrations and the plateau data points of the proxigram (Sudbrack, 2004; Sudbrack et al., 2004). Data points away from the heterophase interface are used to derive the matrix concentrations, where the Fe concentration profile is utilized as a fiducial marker to delineate the plateau region of the proxigram. Only points a distance greater than 1.5 nm away from the heterophase interface with a $\pm\sigma < 0.2$ at.% are included. Therefore, atoms found within the heterophase interface are not included.

[2]One standard deviation for a chemical species i is based on counting statistics and is given by $\sigma_i = \sqrt{[1 - c_i]c_i/N_{TOT}}$, where σ_i is the standard deviation, c_i is the concentration in atomic fraction, and N_{TOT} is the total number of ions.

Results

Figure 1a shows a three-dimensional reconstruction of the entire analyzed volume. Figure 1b shows only the positions of Cu atoms allowing visual detection of the Cu-rich precipitates. The precipitate labeled "A," delineated by the envelope method, is identified and discussed in greater depth below. Figure 1c exhibits 4921 atoms in a 6-nm-diameter region of interest (ROI) that includes the precipitate labeled "A" and the surrounding matrix. The 6-nm-diameter ROI is greater than the precipitate dimensions.

Envelope Methodology

Plotting (Figure 2) the number of clusters as a function of the maximum separation distance between the Cu solute atoms shows the effect of the maximum separation distance on cluster count. When $d_{\max}$ is too small the algorithm cannot identify clusters of three atoms or more ($N_{\min} = 3$), as the separation distance is smaller than the first nearest neighbor distance of the α-Fe (b.c.c.) matrix ($a = 0.287$ nm). The quantity $N_{\min}$ was set at an artificially low value to avoid excluding any possible precipitates. The number of clusters decreases as the separation distance approaches a local minimum at $d_{\max} \cong 0.6$ nm. The number of clusters stays relatively constant as a function of the maximum separation distance from ~0.5 to ~0.7 nm. From ~0.7 nm to $d_{\max} = 1.1$ nm, the number of clusters increases due to the presence of many clusters with only a few atoms. This is possibly due to diffusing solute atoms that are close to one another but have not yet formed a stable precipitate or to trajectory aberrations at diffuse heterophase precipitate/matrix interfaces. Because most of the observed increase is due to small clusters of five atoms or less located away from the heterophase interfaces, the first possibility is most likely. Also observable when $d_{\max}$ is in this range are clusters that are artificially combined. As $d_{\max}$ is increased beyond 1.1 nm, the number of clusters drops dramatically as adjacent clus-

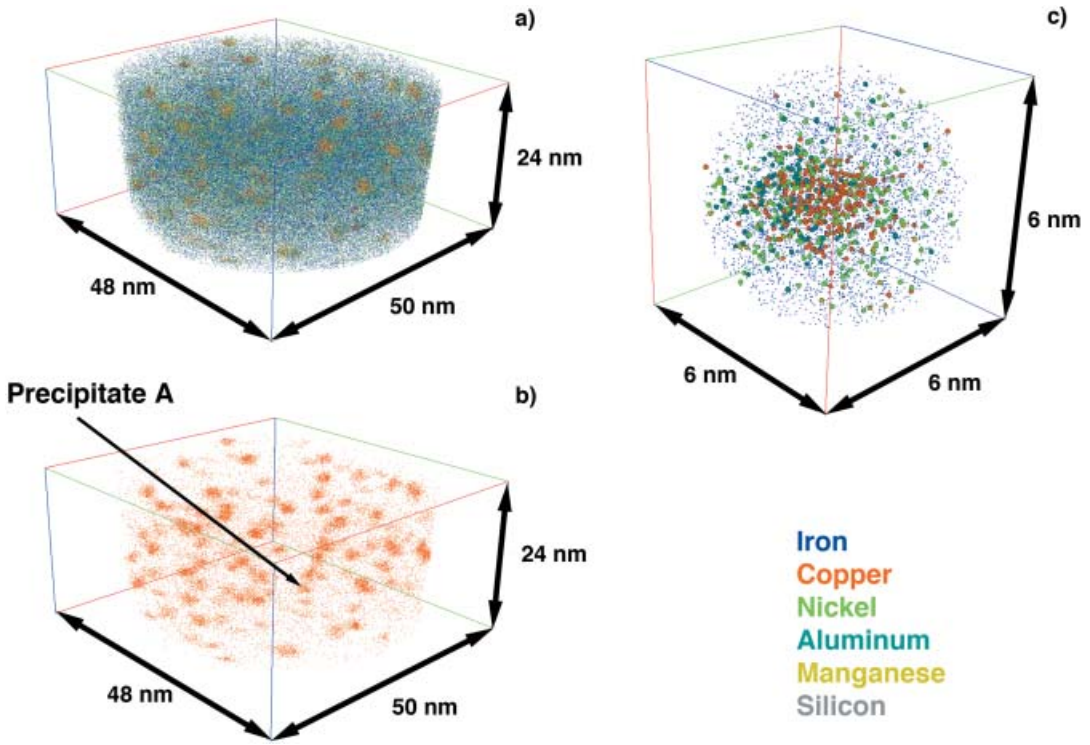

Figure 1. **a:** The analyzed volume of $50 \times 48 \times 24$ nm^3 containing ca. 1.8×10^6 atoms. A reduced number of Fe atoms are shown for clarity. **b:** Positions of Cu atoms allowing visual detection of the Cu-rich precipitates. The precipitate labeled "A," which is delineated by the envelope algorithm, is identified. **c:** A 6-nm-diameter region of interest (ROI) of the precipitate labeled "A" and the surrounding matrix. The 6-nm-diameter ROI contains 4921 total atoms. The Cu, Ni, Al, and Mn atoms are shown enhanced allowing visualization of the precipitate.

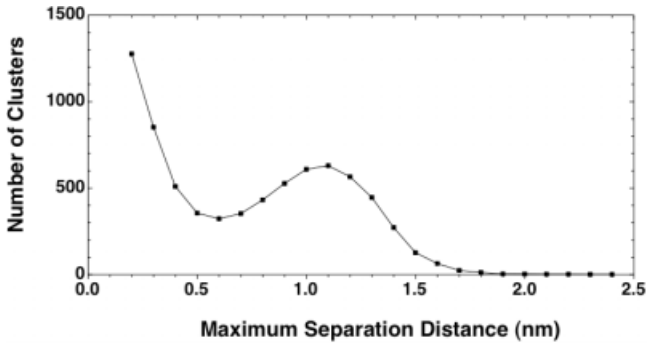

Figure 2. Number of clusters of Cu solute atoms as a function of maximum separation distance between Cu solute atoms with $N_{min} = 3$. A local minimum is seen at ~0.6 nm.

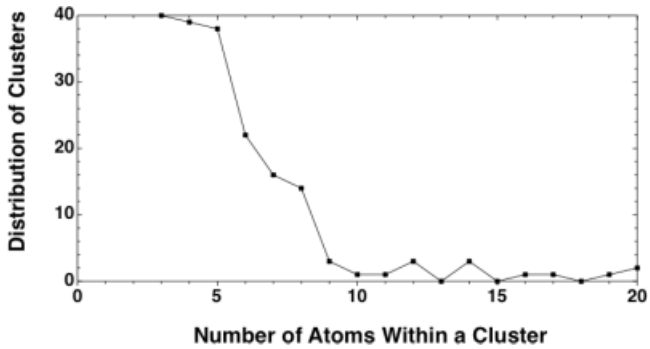

Figure 3. Distribution of clusters as a function of all atoms within a cluster when $d_{max} = 0.6$ nm. The distribution is truncated at 20 atoms.

ters are artificially combined in increasing numbers. At an extreme value of d_{max}, all the clusters are artificially combined into one large feature. The local minimum value, ~0.6 nm, found in the curve corresponds to the correct value of d_{max}, because small deviations from this value do not affect significantly the number of clusters. Additionally, when d_{max} is equal to the local minimum value, we do not find clusters that are artificially combined. Setting $d_{max} =$ 0.6 nm results in 323 clusters of Cu atoms that are potential precipitates.

Figure 3 shows the distribution of clusters as a function of the number of atoms within a cluster when $d_{max} =$ 0.6 nm. A reasonable choice for N_{min} is 10 or 11 atoms, which eliminates clusters containing few atoms and gives a stable number of precipitates, as increasing N_{min} does *not* significantly decrease the number of precipitates. When

$N_{\min} = 10$, then 146 precipitates are delineated, whereas when $N_{\min} = 11$, then 144 precipitates are delineated, giving a precipitate number density, N_V, equal to $(3.8 \pm 0.5) \times 10^{24}$ m^{-3}, where the error is given by counting statistics. When $N_{\min}$ is too small, the number of delineated precipitates increases; conversely, when $N_{\min}$ is too large, the number of precipitates decreases. For example, when $N_{\min} = 5$, then 169 precipitates are delineated and when $N_{\min} = 30$, then 125 precipitates are delineated. Choosing $d_{\max}$ equal to 0.6 nm and $N_{\min}$ equal to 11 atoms results in 6809 excluded clusters containing less than the defined minimum number of atoms. Of these, 6750 contain three atoms or less, suggesting the majority are random fluctuations of solute atoms.

Utilizing a grid spacing of 0.2 nm allows creation of an envelope for each precipitate and the subsequent analysis of morphology and composition of each precipitate. We find that varying the grid spacing by small amounts does not affect significantly the morphological or compositional results. The envelope of the precipitate labeled "A" has an x-dimension of 4.6 nm, a y-dimension of 4.5 nm, and a z-dimension of 1.4 nm. This precipitate contains 225 Cu atoms and 674 total atoms, giving a precipitate volume of 16.0 nm^3 and a value for r_{volume} of 1.6 nm. The value for l_g is equal to 1.0 nm, giving r_{sphere} equal to 1.3 nm, assuming the precipitate is a homogeneous spherical body. Applying the best-fit ellipsoid approximation gives r_{major} equal to 1.89 nm, r_{minor1} equal to 1.47 nm, and r_{minor2} equal to 1.09 nm. The calculated ellipsoid volume is 12.7 nm^3, and the calculated value for $r_{ellipsoid}$ is equal to 1.4 nm. The three ellipsoid radii also give a major/minor$_1$ ratio of 1.29, a major/minor$_2$ ratio of 1.73, and a minor$_1$/minor$_2$ ratio of 1.35. The precipitate labeled "A" has a concentration of 33.4 ± 1.8 Cu, 9.9 ± 1.2 Ni, 5.2 ± 0.9 Al, 0.4 ± 0.3 Mn, 0.6 ± 0.3 Si, and 50.4 ± 1.9 Fe (all in at.%), with the errors given by counting statistics. Figure 4 displays the radial concentration profile for the precipitate labeled "A." We find qualitatively the core of this precipitate is enriched in Cu, Fe, Al, and Ni, whereas Si and Mn are not found within the core of this precipitate. The Cu concentration in the core is 42.3 ± 5.6 at.%, which decreases as the matrix is approached and reaches a relatively constant value at a distance >2.0 nm. The Fe concentration at the core of the precipitate is 50.0 ± 5.7 at.% and increases toward the matrix and, at ca. 2.2 nm, approaches its nominal value. Nickel and Al form similar profiles and, at the core of the precipitate, possess concentrations of 6.4 ± 2.8 at.% and 1.3 ± 1.3 at.%, respectively. From ca. 0.3 to 2.1 nm an elevated concentration of Ni and Al exists, forming a spherical shell. At a distance <0.9 nm Mn is *not* found. From ca. 0.9 to 2.2 nm an elevated concentration of Mn, forming a spherical shell overlapping the Ni and Al profiles, is detected. At distances ca. <1.2 nm Si is not found within one standard deviation.

Scaled PSDs generated from the radii of all 144 precipitates delineated by the envelope algorithm are seen in Figure 5a–c. The value of $\langle l_g \rangle$ in Figure 5a is 1.0 ± 0.01 nm, yielding an $\langle r_{sphere} \rangle$ value of 1.3 ± 0.01 nm, where the error is given by the standard error of the mean. The standard deviation of the distribution is equal to 0.2 nm. The value of $\langle r_{volume} \rangle$ in Figure 5b is 1.2 ± 0.04 nm. The standard deviation of the distribution is equal to 0.4 nm. The value of $\langle r_{ellipsoid} \rangle$ in Figure 5c is 1.3 ± 0.03 nm, where the standard deviation of the distribution is equal to 0.4 nm.

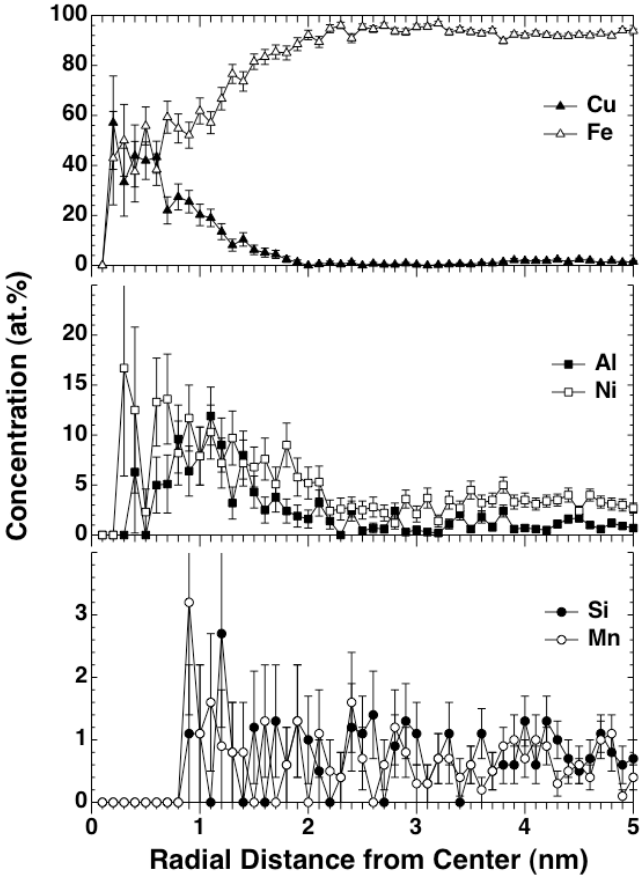

Figure 4. Radial concentration profile from center of mass to 5 nm for the precipitate labeled "A" in Figure 1b using a bin width of 0.1 nm. The error for each concentration is based on counting statistics, $\sigma_i = \sqrt{[(1 - c_i)c_i]/N_{TOT}}$. The larger error bars present toward the center of the precipitate are due to a smaller number of atoms present in each bin.

The composition of all 144 precipitates within the analyzed volume is 35.3 ± 0.2 Cu, 6.9 ± 0.1 Ni, 5.1 ± 0.1 Al, 1.1 ± 0.04 Mn, 0.9 ± 0.04 Si, and 50.7 ± 0.2 Fe (all in at.%), with the errors given by counting statistics. The composition of the matrix is 0.51 ± 0.01 Cu, 3.3 ± 0.01 Ni, 1.2 ± 0.01 Al, 0.6 ± 0.01 Mn, 1.0 ± 0.01 Si, and 93.5 ± 0.02 Fe (all in at.%). Using these values to determine the partitioning ratio, κ_i, for each element, we obtain 69.3 ± 0.9 for Cu, 2.1 ± 0.03 for Ni, 4.4 ± 0.08 for Al, 1.9 ± 0.08 for Mn, 1.0 ± 0.04 for Si, and 0.54 ± 0.002 for Fe, where the error is derived from the concentration errors by standard error propagation methods.

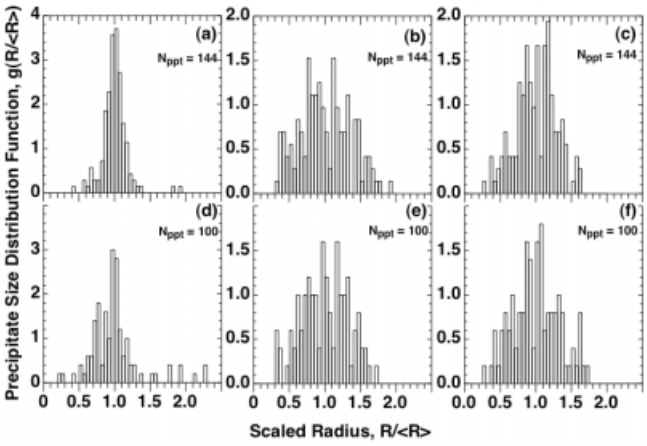

Figure 5. Scaled precipitate size distribution functions (PSDs) as a function of the scaled radius for the precipitates identified by the envelope methodology (**a–c**) and the isoconcentration surface methodology (**d–f**). Bin width is 0.05 $R/\langle R\rangle$. Each PSD is scaled such that the area under the distribution is equal to unity.

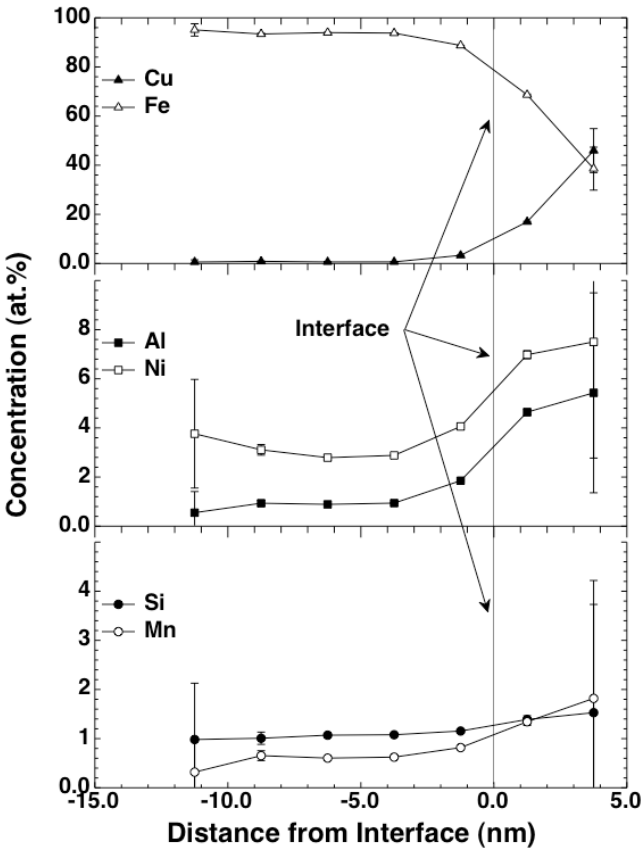

Figure 6. Proxigram concentration profiles for Cu, Fe, Al, Ni, Si, and Mn for all precipitates within the analyzed volume with respect to a 5 at.% Cu isoconcentration surface. Positive values from the heterophase interface delineate the Cu-rich precipitate, whereas negative values delineate the matrix. The error bars are based on the counting statistics, $\sigma_i = \sqrt{[(1-c_i)c_i]/N_{TOT}}$. The larger error bars present at distances far from the heterophase interface are due to a smaller number of atoms present in each bin.

Isoconcentration Surface Methodology

For the HSLC Fe-Cu based steel in this study, a grid spacing of 1 nm, a Gaussian-like spline transfer function, a delocalization distance of 2 nm, a confidence sigma parameter equal to 1, and a $c^{threshold}$ equal to 5.0 at.% Cu are utilized, giving 100 isoconcentration surfaces delineating precipitates. The number density, N_V, is equal to $(2.6 \pm 0.6) \times 10^{24}$ precipitates m^{-3}, where the error is given by counting statistics. This value of concentration threshold gives morphologically stable results, meaning small changes do not significantly affect the number or dimensions of the precipitates. The remaining parameters are chosen to balance positional values and statistical error obtaining noise-free isoconcentration surfaces. The ratio of the delocalization distance to grid spacing is maintained at 2:1. The atoms within the delineated precipitates were selected and exported from the Adam 1.5 program and imported into the IVAS program to determine the dimensions of the precipitates with the latter program.

Scaled PSDs generated from the radii of all 100 precipitates delineated by the isoconcentration surface methodology are seen in Figure 5d–f. The value of $\langle l_g \rangle$ in Figure 5d is 1.0 ± 0.03 nm, yielding an $\langle r_{sphere} \rangle$ value of 1.3 ± 0.04 nm, where the error is given by the standard error of the mean. The standard deviation of the distribution is equal to 0.3 nm. The value of $\langle r_{volume} \rangle$ in Figure 5e is 1.4 ± 0.04 nm. The standard deviation of the distribution is equal to 0.4 nm. The value of $\langle r_{ellipsoid} \rangle$ in Figure 5f is 1.3 ± 0.04 nm, where the standard deviation of the distribution is equal to 0.4 nm.

Figure 6 shows the proxigram concentration profiles generated from the reference isoconcentration surfaces. The centers of the precipitates delineated by the rightmost data point for this figure is enriched in Cu at a concentration of 45.9 ± 9.0 at.%, which decreases toward the heterophase interface and reaches a matrix concentration derived from the plateau data points of 0.6 ± 0.01 at.% Cu. The centers of the precipitates also contain a high level of Fe at a concentration of 38.6 ± 8.7 at.%, increasing to the nominal concentration of 93.8 ± 0.03 at.% in the matrix. We find qualitatively that the cores of the precipitates are enriched in Ni, Al, Mn, and Si. Nickel and Al form similar profiles, and the core of the precipitates possesses concentrations of 7.0 ± 1.7 at.% and 4.6 ± 1.4 at.%, respectively. The concentration of each element decreases in the matrix to 2.9 ± 0.02 at.% for Ni and 0.9 ± 0.01 at.% for Al. The concentration of Mn at the core is 1.3 ± 0.1 at.%, which decreases to 0.6 ± 0.01 at.% in the matrix. The concentration of Si is 1.4 ± 0.1 at.% in the core, which decreases to 1.0 ± 0.01 at.% in the matrix. Using these concentration values to

determine the partitioning ratio, κ_i, for each element we obtain 26.4 ± 0.5 for Cu, 2.4 ± 0.06 for Ni, 5.0 ± 0.2 for Al, 2.2 ± 0.1 for Mn, 1.3 ± 0.07 for Si, and 0.73 ± 0.003 for Fe, where the error is derived from the concentration errors by standard error propagation methods.

Discussion

The envelope methodology depends on differences in solute atom spacing between the precipitate and matrix phases. The dimensions and number of precipitates within the analyzed volume and the accuracy and precision in defining the precipitate/matrix heterophase interfaces are dependent on the choice of the quantities $d_{\max}$ and $N_{\min}$. The value of both parameters is dependent on the system studied, but the technique utilized in this investigation can be applied to any multicomponent system. We emphasize that the value for $d_{\max}$, 0.6 nm, found at the aging condition in this study remains relatively constant at other aging times for this HSLC Fe-Cu based steel. For example, when the steel is aged for 4 h, we find that $d_{\max}$ is equal to 0.5 nm, and when the steel is aged for 1024 h we find that $d_{\max}$ is equal to 0.6 nm. Aging for times greater than 4 h or less than 1024 h results in similar values. The value for $N_{\min}$ is also relatively constant at aging times less than 256 h. For example in a steel aged for 64 h varying $N_{\min}$ from 10 to 30 Cu atoms results in a variation of 6 precipitates. At an aging time of 1024 h, however, the choice of $N_{\min}$ is complicated by the wider heterophase precipitate/matrix interfaces of the large precipitates. Choosing a value for $N_{\min}$ between 10 and 30 Cu atoms identifies correctly the precipitates but also delineates a number of small precipitates located at the heterophase interfaces, which is an artifact of the interface width. The quantity $N_{\min}$ must be increased to 100 atoms to eliminate the incorrectly identified artifact precipitates.

The isoconcentration surface methodology relies on concentration variations and a threshold value rather than solute atom spacing differences. The isoconcentration surface can therefore identify precipitates in almost all alloys, but, as discussed above, the choice of user-defined parameters, such as grid spacing, smoothing transfer function, delocalization distance, and confidence sigma value, affect both positional values and statistical errors. We find that for the utilized transfer function, a Gaussian-like spline, small changes to the other three parameters do not affect significantly the results. If, however, the ratio of delocalization distance to grid spacing is made greater than 4:1, some adjacent precipitates are artificially connected. The dimensions and number of precipitates within the analyzed volume and the accuracy and precision in defining the precipitate/matrix heterophase interfaces is dependent on the choice of $c^{threshold}$. The selection of the quantity $c^{threshold}$ is dependent on the system studied and composition of the precipitate. We emphasize, however, that utilizing a $c^{threshold}$ equal to 5 at.% Cu identifies correctly precipitates at other aging times for this HSLC Fe-Cu based steel.

Due to the inherent differences in defining precipitates in a given matrix, the different extant methods did not produce the same quantitative results. The envelope methodology (Miller, 2000*a*, 2000*b*; Miller & Kenik, 2004) identifies 44 more precipitates than the isoconcentration surface methodology (Hellman et al., 2000, 2002, 2003). The resulting number density, $(3.8 \pm 0.5) \times 10^{24}$ m^{-3}, found from the envelope methodology is a factor of 1.46 greater than the number density, $(2.6 \pm 0.6) \times 10^{24}$ m^{-3}, found from the isoconcentration surface methodology. The difficulty in choosing a concentration threshold value corresponding to a maximum separation distance, which is essentially an iterative process, prevents an exact correlation of results. Sensitivity of the number of precipitates to the distance $d_{\max}$ in the envelope algorithm and to the quantity $c^{threshold}$ in the isoconcentration surface methodology means that convergence of precipitate quantities is possible. There is, however, no *a priori* reason for the two methodologies to obtain the exact same results, as their original premises are different.

Examination of the 44 precipitates identified by the envelope algorithm but *not* the isoconcentration surface methodology reveals that some are at the boundaries of the analyzed volume whereas others are found in the interior; both types, though, contain fewer Cu atoms than the precipitates identified by the isoconcentration surfaces. These precipitates are most likely fractions of whole precipitates or larger embryos that are not eliminated by the choice of $N_{\min}$. Those precipitates found at the boundary of the analyzed volume may represent parts of true precipitates or the edges of artificially diffuse heterophase interfaces resulting from possible trajectory aberrations. Increasing the value of $N_{\min}$ reduces the number of these types of precipitates, but too large an increase in $N_{\min}$ can eliminate genuine small precipitates located wholly within the analyzed volume. The isoconcentration surface methodology excludes these types of precipitates by the use of a confidence sigma value, which eliminates effectively isoconcentration surfaces below the selected statistical uncertainty (Hellman et al., 2003). Both techniques identify successfully the same larger precipitates at the boundary of the analyzed volume.

Precipitate Morphology

One must understand the advantages and limitations of estimating the dimensions of a precipitate using the different radii. The results presented herein provide four different values for the radius of the precipitate labeled "A," identified by the envelope method, ranging from a radius of gyration of 1.0 nm to a r_{volume} equal to 1.6 nm. The value of l_g gives r_{sphere} equal to 1.3 nm for an assumed spherical shape. An effective ellipsoid radius of 1.4 nm is also found.

Estimating the volume from equation (1) is most accurate for alloys where the precipitate and matrix phases have similar lattice spacings. Using this volume to determine the

quantity r_{volume} is clearly most accurate for spherical homogeneous precipitates; that is, the solute species are distributed uniformly within the precipitates. An advantage of using this radius is that morphological artifacts resulting from local magnification effects (Miller, 2000*a*), known to occur in Fe-Cu based steels and discussed in greater detail below, do not affect the result.

The quantity l_g represents a physical dimension but is related to the moment of inertia of the precipitates. As mentioned above it does *not* represent the actual physical extent of a precipitate and underestimates the dimensions of a precipitate. Using the radius of gyration to calculate r_{sphere} is most accurate for spherical homogeneous precipitates. The radii l_g and r_{sphere} also have the disadvantage of a dependence on the *x*-, *y*-, and *z*-positions of the reconstructed atoms, which, as discussed below, may be affected by the local magnification effect.

The quantity $r_{ellipsoid}$ can characterize precipitates that have a prolate spheroidal morphology, that is, elongated precipitates. In extreme cases, such as model binary Fe-Cu and ternary Fe-Cu-Ni alloys aged for longer times or at higher temperatures, where the precipitates grow preferentially along the low-energy $[110]_{Cu}$ interface direction (Hornbogen & Glenn, 1960; Speich & Oriani, 1965; Othen et al., 1991, 1994), $r_{ellipsoid}$ most likely provides a more accurate representation of the dimensions of a precipitate than do the quantities r_{volume}, r_{sphere}, or l_g. In the HSLC Fe-Cu based steel used in this study, the aging condition results, however, in precipitates with smaller dimensions that are spheroidal rather than ellipsoidal. For this reason, use of the quantity $r_{ellipsoid}$ is not appropriate for the HSLC Fe-Cu based steel in the aging condition studied. The observed slight elongation of a few precipitates in the *z*-direction is possibly a result of local magnification effects.

We emphasize that any radius determined from the reconstructed positions of the atoms, such as l_g, r_{sphere}, and $r_{ellipsoid}$, would be affected by the local magnification effect, which, due to the differences in the observed evaporation fields of Cu-rich (30 V nm^{-1}) precipitates and Fe-rich (36 V nm^{-1}) matrix, are known to occur in Fe-Cu based steels (Müller & Tsong, 1969; Goodman et al., 1973*a*; Tsong, 1990). An approximation to correct the radius, however, is given by

$$r^{corrected} = r\sqrt{\frac{n_p}{n_m}}, \tag{7}$$

where r is the determined radius, and n_j ($j = p$ or m) is the number of atoms within a unit volume for the precipitate and matrix phases (Miller, 2000*a*), respectively. In the aging condition studied for the HSLC Fe-Cu based steel, however, the precipitates still contain significant quantities of Fe, and the quantity $\sqrt{n_p/n_m}$ is close to unity. Additionally, because we observe the elongation of only a few precipitates, we compare the as-determined radius, r_{sphere}, with r_{volume}, without applying the correction from equation (7).

Excluding the radii $\langle l_g \rangle$ and $\langle r_{ellipsoid} \rangle$ from the PSD results of Figure 5a–c and comparing only the radii $\langle r_{sphere} \rangle$ and $\langle r_{volume} \rangle$, the difference is 0.1 nm, which is ~8%. These values are reasonably close to those obtained from PSDs using results from the isoconcentration surface methodology, displayed in Figure 5d–f. Again not including the quantities $\langle l_g \rangle$ or $\langle r_{ellipsoid} \rangle$, the difference is 0.1 nm, which is ~8%. As seen from the above discussion, a judicious selection of the parameters employed by the two methods (maximum separation distance and minimum number of solute atoms vs. a concentration threshold) results in similar precipitate radii. We emphasize that the similarity of results occurs after applying the two techniques independently, indicating that either methodology could be utilized to generate PSDs and determine the mean radius of the precipitates within an analyzed volume.

Precipitate Composition

It is important that, despite the technical differences between the two precipitate identification methodologies and the two concentration profiles, the results are qualitatively similar and correlate well to other studies of Fe-Cu based steels. The results demonstrate that the precipitates within the analyzed volume are enriched in Cu and contain Fe. The presence of Fe in Cu-rich precipitates at shorter aging times has been debated in the literature since Goodman et al.'s (1973*a*, 1973*b*) pioneering atom-probe field ion microscopy (APFIM) studies on a binary Fe-Cu steel. Subsequent studies have not fully decided the issue (Kampmann & Wagner, 1986; Worrall et al., 1987; Miller et al., 2003; Isheim et al., 2006*a*), and no attempt is made herein to resolve this matter. The Ni, Al, and Mn enhancement surrounding the Cu-rich core and the nonmonotonic profiles seen in both Figures 4 and 6 is also observed by experiments and simulations in similar model Fe-Cu based steels containing two to four components (Watanabe, 1975; Worrall et al., 1987; Osamura et al., 1994; Pareige et al., 1996; Koyama & Onodera, 2005; Isheim et al., 2006*a*, 2006*b*).

The primary difference between the proxigram (Hellman et al., 2000) and radial concentration profiles is that the former is created with respect to an isoconcentration surface delineating the precipitate/matrix heterophase interfaces, whereas the latter profile uses the COM as the reference point and then draws the profiles. A second difference is the spherical shape assumption of the radial concentration profile, which limits its usefulness for elongated precipitates. If the precipitates are elongated, then spherical binning of atoms does *not* provide an accurate concentration profile, because matrix atoms are included along the shortest principal axis. An additional difficulty is defining the precipitate/matrix chemical heterophase interface, which may not correspond with the precipitate/matrix morphological boundary as defined by the precipitate radius. Although

subject to the choice of the solute atom, the definition of the chemical width of a heterophase interface is inherent within the proxigram.

Independently of the technical differences among the methods, it is important that the qualitative result of the proxigram concentration profiles (Fig. 6) and the radial concentration profiles (Fig. 4) are similar. Both exhibit high concentrations of Cu and Fe at the centers of precipitates, and good agreement is observed for the Cu, Fe, Ni, and Al profiles. The quantitative agreement is not as good with a difference of ca. 3.6 at.% Cu, ca. 11.4 at.% Fe, ca. 0.6 at.% Ni, and ca. 3.3 at.% Al. The proxigram profile shows the presence of Mn and Si, whereas, as discussed above, the radial profile shows depletion of these elements. These variations are attributed to the differences between a superimposed average concentration profile versus a concentration profile for a single precipitate. We emphasize that although both concentration profiles have larger error bars at data points toward the center of the precipitate, which is a result of the smaller number of atoms present in these bins, the qualitative similarity of the profiles suggests that both methodologies provide reasonable results.

Comparison of the partitioning ratios shows reasonably similar values for Ni, Al, Mn, and Si. Although the Si values are close, the results from the envelope methodology demonstrate that Si does not partition to either the precipitate or matrix, whereas the results from the isoconcentration surface methodology show Si partitioning slightly to the precipitate. Both techniques give the same qualitative results for Cu and Fe: Cu partitions strongly to the precipitate whereas Fe prefers the matrix. The quantitative values are, however, significantly different, especially for Cu. Possible reasons for the observed variations are the envelope method's inclusion of atoms found at the heterophase interface, different bin sizes in the two different methodologies determining κ_i, and/or inclusion of some heterophase interface atoms in determining the precipitate core concentrations from the proxigram.

Conclusions

Local-electrode atom-probe (LEAP) tomography data obtained from a multicomponent HSLC Fe-Cu based steel solutionized at 900°C, quenched into water at 25°C, and then aged for 1 h at 500°C is studied using two different methodologies for the identification of precipitates. The precipitates are first identified using a maximum separation distance algorithm, the envelope method, and then by a compositional threshold method, an isoconcentration surface. The morphological and compositional results of applying the two methodologies are compared. The results show quantitative differences in the number of precipitates identified due to technical differences in the basis of both methods and the sensitivity of the results to user-prescribed parameters. The morphology of the precipitates, characterized by four different precipitate radii and precipitate size distribution functions, are compared and evaluated. A variation of less than ~8% is found between the different radii. The mean composition of the precipitates, using two types of concentration profiles and partitioning ratios, yields qualitatively similar results. Both the proximity histogram and radial concentration profiles exhibit Cu-rich precipitates containing Fe with elevated concentrations of Ni, Al, and Mn near the heterophase precipitate/matrix interfaces. There are, however, quantitative disagreements due to differences in the basic foundations of the analysis methods. The resulting partitioning ratios are also qualitatively similar but with quantitative differences for Fe and Cu between the two analysis methods.

Acknowledgments

This research is supported by the Office of Naval Research (N00014-03-1-0252), Dr. Julie Christodoulou grant officer. Atom-probe tomographic analyses were performed at the Northwestern University Center for Atom-Probe Tomography (NUCAPT), and the LEAP tomograph was purchased with funding from the NSF-MRI (DMR-0420532, Dr. Charles Bouldin, monitor) and ONR-DURIP (N00014-0400798, Dr. Julie Christodoulou, monitor) programs. Research Professor Dieter Isheim is kindly thanked for managing NUCAPT and reading the manuscript. Richard Karnesky is kindly thanked for reading the manuscript. Dr. Shrikant Bhat of Mittal Steel USA Research Center is kindly thanked for supplying the HSLC steel used in this study.

References

Al-Kassab, T. (2002). *Exploring the Nano-structure in Metals: Analyses with the Tomographic Atom Probe*. University of Göttingen: Habilitationschrift.

Christian, J.W. (2002). *The Theory of Transformation in Metals and Alloys, Vol. 1*. Amsterdam: Pergamon Press.

de Geuser, F., Lefebvre, W. & Blavette, D. (2006). 3D atom probe study of solute atoms clustering during natural aging and pre-aging of an Al-Mg-Si alloy. *Philos Mag Let* **86**, 227–234.

Fultz, B. & Howe, J.M. (2002). *Transmission Electron Microscopy and Diffractometry of Materials*. Berlin: Springer.

Goodman, S.R., Brenner, S.S. & Low, J.R., Jr. (1973*a*). An FIM-atom probe study of the precipitation of copper from iron-1.4 at. pct. copper. Part I: Field-ion microscopy. *Metall Trans* **4**, 2363–2369.

Goodman, S.R., Brenner, S.S. & Low, J.R., Jr. (1973*b*). An FIM-atom probe study of the precipitation of copper from iron-1.4 at. pct. copper. Part II: Atom probe analyses. *Metall Trans* **4**, 2371–2378.

Guinier, A. (1963). *X-Ray Diffraction*. San Francisco: W. H. Freeman and Company.

Heinrich, A., Al-Kassab, T. & Kirchheim, R. (2003). Investigation of the early stage of decomposition of Cu-0.7 at.% Fe with the tomographic atom probe. *Mater Sci Eng* **A353**, 92–98.

Hellman, O.C., Blatz du Rivage, J. & Seidman, D.N. (2003). Efficient sampling for three-dimensional atom probe microscopy data. *Ultramicroscopy* **95**, 199–205.

Hellman, O.C., Vandenbroucke, J.A., Blatz du Rivage, J. & Seidman, D.N. (2002). Application software for data analysis for three-dimensional atom probe microscopy. *Mater Sci Eng* **A327**, 29–33.

Hellman, O.C., Vandenbroucke, J.A., Rüsing, J., Isheim, D. & Seidman, D.N. (2000). Analysis of three-dimensional atom-probe data by the proximity histogram. *Microsc Microanal* **6**, 437–444.

Hibbler, R.C. (2001). *Engineering Mechanics, Statics & Dynamics*. Upper Saddle River, NJ: Prentice-Hall.

Hornbogen, E. & Glenn, R.C. (1960). A metallographic study of precipitation of copper from alpha iron. *Trans Metall Soc AIME* **218**, 1064–1070.

Hyde, J.M. (1993). Computer modeling analysis of microscale phase transformations. Ph.D. dissertation. Oxford: University of Oxford.

Hyde, J.M. & English, C.A. (2000). An analysis of structure of irradiation induced Cu-enriched clusters in low and high nickel welds. *Mat Res Soc Symp Proc* **650**, R6.6.1–R.6.6.12.

Isheim, D., Gagliano, M.S., Fine, M.E. & Seidman, D.N. (2006*a*). Interfacial segregation at Cu-rich precipitates in a high-strength low-carbon steel studied on a sub-nanometer scale. *Acta Mater* **54**, 841–849.

Isheim, D., Kolli, R.P., Fine, M.E. & Seidman, D.N. (2006*b*). An atom-probe tomographic study of the temporal evolution of the nanostructure of Fe-Cu based high-strength low-carbon steels. *Scripta Mater* **55**, 35–40.

Kampmann, R. & Wagner, R. (1986). *Phase Transformations in Fe-Cu-Alloys—SANS—Experiments and Theory*. In *Atomic Transport and Defects in Metals by Neutron Scattering*, Janot, C., Petry, W., Richter, D. & Springer, T. (Eds.), vol. 10. Berlin: Springer-Verlag.

Karnesky, R.A., Sudbrack, C.K. & Seidman, D.N. (2007). Best-fit ellipsoids of atom-probe tomographic data to study coalescence of γ' ($L1_2$) precipitates in Ni-Al-Cr. *Scripta Mater* **57**, 353–356.

Kelly, T.F., Camus, P.P., Larson, D.J., Holzman, L.M. & Bajikar, S.S. (1996). On the many advantages of local-electrode atom probes. *Ultramicroscopy* **62**, 29–42.

Kelly, T.F., Gribb, T.T., Olson, J.D., Martens, R.L., Shepard, J.D., Wiener, S.A., Kunicki, T.C., Ulfig, R.M., Lenz, D.R., Strennen, E.M., Oltman, E., Bunton, J.H. & Strait, D.R. (2004). First data from a commercial local electrode atom probe (LEAP). *Microsc Microanal* **10**, 373–383.

Kelly, T.F. & Larson, D.J. (2000). Local electrode atom probes. *Mater Charac* **44**, 59–85.

Kluthe, C., Al-Kassab, T. & Kirchheim, R. (2003). Early stages of oxide precipitation in Ag-0.42at.%-Mg-examined with the tomographic atom probe. *Mater Sci Eng* **A353**, 112–118.

Koyama, T. & Onodera, H. (2005). Computer simulation of phase decomposition in Fe-Cu-Mn-Ni quaternary alloy based on the phase-field method. *Mater Trans* **46**, 1187–1192.

Krakauer, B.W., Hu, J.G., Kuo, S.-M., Mallick, R.L., Seki, A. & Seidman, D.N. (1990). A system for systematically preparing atom-probe field-ion microscope specimens for the study of internal interfaces. *Rev Sci Instrum* **61**, 3390–3398.

Krakauer, B.W. & Seidman, D.N. (1992). Systematic procedures for atom-probe field-ion microscopy studies of grain boundary segregation. *Rev Sci Instrum* **63**, 4071–4079.

Meyer, S.L. (1975). *Data Analysis for Scientists and Engineers*. New York: John Wiley & Sons, Inc.

Miller, M.K. (2000*a*). *Atom Probe Tomography*. New York: Kluwer Academic/Plenum Publishers.

Miller, M.K. (2000*b*). Characterization of the early stages of phase separation by atom probe tomography. *Mat Res Soc Symp Proc* **580**, 35–40.

Miller, M.K. & Kenik, E.A. (2004). Atom probe tomography: A technique for nanoscale characterization. *Microsc Microanal* **10**, 336–341.

Miller, M.K., Wirth, B.D. & Odette, G.R. (2003). Precipitation in neutron-irradiated Fe-Cu and Fe-Cu-Mn model alloys: A comparison of APT and SANS data. *Mater Sci Eng* **A353**, 133–139.

Müller, E.W. & Tsong, T.T. (1969). *Field Ion Microscopy*. New York: American Elsevier Publishing Company, Inc.

Osamura, K., Okuda, H., Asano, K., Furusaka, M., Kishida, K., Kurosawa, F. & Uemori, R. (1994). SANS study of phase decomposition in Fe-Cu alloy with Ni and Mn addition. *ISIJ Int* **34**, 346–354.

Othen, P.J., Jenkins, M.L. & Smith, G.D.W. (1994). High-resolution electron microscopy studies of the structure of Cu precipitates in alpha-Fe. *Philos Mag A* **70**, 1–24.

Othen, P.J., Jenkins, M.L., Smith, G.D.W. & Phythian, W.J. (1991). Transmission electron microscope investigations of the structure of copper precipitates in thermally-aged Fe-Cu and Fe-Cu-Ni. *Philos Mag Let* **64**, 383–391.

Pareige, P.J., Russell, K.F. & Miller, M.K. (1996). APFIM studies of the phase transformation in thermally aged ferritic FeCuNi alloys: Comparison with aging under neutron irradiation. *Appl Surf Sci* **94/95**, 362–369.

Ratke, L. & Voorhees, P.W. (2002). *Growth and Coarsening*. Berlin: Springer.

Speich, G.R. & Oriani, R.A. (1965). The rate of coarsening of copper precipitate in an alpha-iron matrix. *Trans Metall Soc AIME* **233**, 623–631.

Sudbrack, C.K. (2004). Decomposition behavior in model Ni-Al-Cr-X superalloys: Temporal evolution and compositional pathways on a nanoscale. Ph.D. thesis. Evanston, IL: Northwestern University.

Sudbrack, C.K., Isheim, D., Noebe, R.D., Jacobson, N.S. & Seidman, D.N. (2004). The influence of tungsten on chemical composition of a temporally evolving nanostructure of a model Ni-Al-Cr superalloy. *Microsc Microanal* **10**, 355–365.

Sudbrack, C.K., Noebe, R.D. & Seidman, D.N. (2006*a*). Direct observation of nucleation in a dilute multicomponent alloy. *Phys Rev B* **73**, 212101.

Sudbrack, C.K., Noebe, R.D. & Seidman, D.N. (2007). Compositional pathways and capillary effects during isothermal precipitation in a nondilute Ni-Al-Cr alloy. *Acta Mater* **55**, 119–130.

Sudbrack, C.K., Yoon, K.E., Noebe, R.D. & Seidman, D.N. (2006*b*). Temporal evolution of the nanostructure and phase compositions in a model Ni-Al-Cr alloy. *Acta Mater* **54**, 3199–3210.

Tsong, T.T. (1990). *Atom-Probe Field Ion Microscopy*. Cambridge: Cambridge University Press.

Vaumousse, D., Cerezo, A. & Warren, P.J. (2003). A procedure for quantification of precipitate microstructures from three-dimensional atom probe data. *Ultramicroscopy* **95**, 215–221.

Vaynman, S., Fine, M.E. & Bhat, S.P. (2004*a*). *High-Strength, Low-Carbon, Ferritic, Copper-Precipitation-Strengthening Steels for Tank Car Applications*, vol. 1, p. 417. New Orleans, LA: AIST and TMS.

Vaynman, S., Fine, M.E., Lee, S. & Espinosa, H.D. (2006). Effect of strain rate and temperature on mechanical properties and fracture mode of high strength precipitation hardened ferritic steels. *Scripta Mater* **55**, 351–354.

Vaynman, S., Isheim, D., Fine, M.E., Seidman, D.N. & Bhat, S.P. (2004*b*). *Recent Advances in High-Strength, Low-Carbon, Precipitation-Strengthened Ferritic Steels*, vol. 1, p. 525. New Orleans, LA: AIST and TMS.

Vurpillot, F., de Geuser, F., Da Costa, G. & Blavette, D. (2004). Application of Fourier transform and autocorrelation to cluster identification in the three-dimensional atom probe. *J Microsc* **216**, 234–240.

Watanabe, T. (1975). Aging of 1%Cu-3%Ni-1%Al steel. *Tetsu-To-Hagane/Journal of the Iron and Steel Institute of Japan* **61**, 2456–2466.

Wolde-Giorgis, D., Al-Kassab, T. & Kirchheim, R. (2003). Nucleation and growth in Cu-0.7at.% Ti as studied with the tomographic atom probe. *Mater Sci Eng* **A353**, 152–157.

Worrall, G.M., Buswell, J.T., English, C.A., Hetherington, M.G. & Smith, G.D.W. (1987). A study of the precipitation of copper particles in a ferrite matrix. *J Nucl Mat* **148**, 107–114.

Yoon, K.E. (2004). Temporal evolution of the chemistry and nanostructure of multicomponent model Ni-based superalloys. Ph.D. thesis. Evanston, IL: Northwestern University.

Yoon, K.E., Noebe, R.D. & Seidman, D.N. (2007*a*). Effects of rhenium addition on the temporal evolution of the nanostructure and chemistry of a model Ni-Cr-Al superalloy, I. Experimental observations. *Acta Mater* **55**, 1145–1157.

Yoon, K.E., Noebe, R.D. & Seidman, D.N. (2007*b*). Effects of rhenium addition on the temporal evolution of the nanostructure and chemistry of a model Ni-Cr-Al superalloy, II. Analysis of the coursening behavior. *Acta Mater* **55**, 1159–1169.